

LOCATING THE YOUNGEST H II REGIONS IN M82 WITH 7 mm CONTINUUM MAPS

CHAO-WEI TSAI¹, JEAN L. TURNER¹, SARA C. BECK², DAVID S. MEIER^{3,6}, AND PAUL T. P. HO^{4,5}

¹ Department of Physics and Astronomy, UCLA, Los Angeles, CA 90095-1547, USA; cwtsai@astro.ucla.edu, turner@astro.ucla.edu

² Department of Physics and Astronomy, Tel Aviv University, Ramat Aviv, Israel; sara@wise1.tau.ac.il

³ Jansky Fellow: National Radio Astronomy Observatory, P. O. Box 0, Socorro, NM 87801, USA; dmeier@nmt.edu

⁴ Harvard-Smithsonian Center for Astrophysics, Cambridge, MA 02138, USA; ho@cfa.harvard.edu

⁵ Institute of Astronomy and Astrophysics, Academia Sinica, PO Box 23-141, Taipei 106, Taiwan

Received 2008 October 3; accepted 2009 March 7; published 2009 April 23

ABSTRACT

We present 7 mm Very Large Array continuum images of the starburst galaxy M82. On arcsecond scales, two-thirds of the 7 mm continuum consists of free–free emission from H II regions. In the subarcsecond resolution map, we identify 14 compact sources, including 9 bright H II regions with $N_{\text{lyc}} > 10^{51} \text{ s}^{-1}$. Four of the H II regions have rising spectra, implying emission measures $> 10^8 \text{ cm}^{-6} \text{ pc}$. Except for one compact source with peculiar features, all other compact radio sources are found in dust lanes and do not have optical or near-infrared continuum counterparts. Four regions of extended, high brightness ($\text{EM} > 10^7 \text{ cm}^{-6} \text{ pc}$) radio emission are found in our high-resolution map, including some as large as $\sim 2''$, or 30 pc, representing either associations of small H II regions, or sheet-like structures of denser gas. The good correlation between 7 mm emission and *Spitzer* IRAC 8 μm continuum-removed polycyclic aromatic hydrocarbon (PAH) feature suggests that PAH emission may track the recently formed OB stars. We find an excellent correlation between molecular gas and star formation, particularly dense gas traced by HCN, down to the $\sim 45 \text{ pc}$ scale in M82. We also find star formation efficiencies (SFEs) of 1%–10% on the same scale, based on CO maps. The highest SFE are found in regions with the highest dense gas fractions.

Key words: galaxies: individual (M 82, NGC 3034) – galaxies: ISM – galaxies: starburst – galaxies: star clusters – H II regions – radio continuum: galaxies

1. INTRODUCTION

Free–free emission from H II regions at radio wavelengths is a good tracer of young and heavily embedded regions of massive star formation such as luminous starbursts and nuclear star-forming regions, where visual extinctions can be tens (Ho et al. 1990) to hundreds of magnitudes, affecting even near-infrared (NIR) and mid-infrared (MIR) observations. Extragalactic continuum emission is complicated by the presence of nonthermal synchrotron emission within the beam, particularly at wavelengths longer than 6 cm (Condon 1992). While it is possible in theory to do a spectral and spatial separation of free–free and synchrotron emission (Turner & Ho 1983, 1994; McDonald et al. 2002) with multiwavelength observations, the free–free emission can be most easily measured at millimeter wavelengths, where radio synchrotron has declined and dust has not yet begun to take over. The enhanced high-frequency capabilities of the Very Large Array (VLA)—improved *K*- and *Q*-band receivers, fast-switching calibration techniques—allow us to detect and resolve the free–free emission from large H II regions in nearby galaxies.

We report VLA observations of the 7 mm continuum emission of the starburst galaxy M82. An interacting dwarf with a bar and gas ring in the central kpc (Telesco et al. 1991; Larkin et al. 1994; Achtermann & Lacy 1995; Shen & Lo 1995), M82 is a prodigious former of stars, at a rate of $\sim 10 M_{\odot} \text{ yr}^{-1}$ (Telesco 1988). The burst of star formation may have been triggered by the interaction with M81 (Yun et al. 1993), or by infalling molecular gas driven by the stellar bar (Greve et al. 2002). Its current active star formation can be traced back to 50 Myr ago (de Grijs 2001). The strong star formation activity is probably

responsible for the hot gas outflows found in optical, mm, and X-ray studies (O’Connell & Mangano 1978; Nakai et al. 1987; Loiseau et al. 1990; Matsumoto et al. 2000; Matsushita et al. 2000; Stevens et al. 2003).

Our goal is to use the 7 mm maps to isolate compact H II regions in M82, and to determine their free–free flux density, from which we can infer Lyman continuum rates, or N_{lyc} . With the subarcsecond resolution afforded by the VLA we can determine locations and sizes of the bright H II regions on scales of a few pc. Extinction is high and patchy in M82 (Simon et al. 1979), estimated to be $A_V \sim 50$ (Förster Schreiber et al. 2001) on large scales, and as much as several hundred mag behind the molecular clouds (Keto et al. 2005), thus radio free–free emission is a particularly valuable tracer of ionized gas in this dusty starburst galaxy.

Spectral energy distributions (SEDs) of the compact radio sources at longer, cm wavelengths (Wills et al. 1997; Allen & Kronberg 1998; Allen 1999; McDonald et al. 2002) in M82 have shown them to be mostly nonthermal synchrotron sources, probably supernova remnants (SNRs) but possibly synchrotron-emitting wind driven bubbles (Seaquist & Stanković 2007). The structures and the expansion properties of these nonthermal sources have been revealed by Very Long Baseline Interferometry (VLBI) and Multi-Element Radio Linked Interferometry (MERLIN) with 3–35 mas resolutions and multiepoch monitoring at 18 and 6 cm (Pedlar et al. 1999; McDonald et al. 2001; Beswick et al. 2006; Fenech et al. 2008). In addition to the radio continuum work, Rodriguez-Rico et al. (2004) studied the H92 α and H52 α radio recombination lines in M82, including the 7 mm (42.952 GHz) continuum, in 0.6 or $\sim 10 \text{ pc}$ resolution.

In this paper, we have 7 mm images at two resolutions: high resolution, 0.2, for compact structures on scales of 3 pc, and low resolution, 1.5, for structures on scales of $\gtrsim 25 \text{ pc}$. The map with 0.2 synthesized beam is the highest resolution map of

⁶ Current address: Department of Physics, New Mexico Institute of Mining Technology, Socorro, NM 87801, USA.

M82 at millimeter wavelengths so far. Lower-resolution maps are important for judging the amount of missing, undersampled emission in higher-resolution VLA images, which act as spatial high-pass filters.

The distance to M82 was recently determined to be 3.6 ± 0.3 Mpc from the optical study of Cepheids in M81 using the *Hubble Space Telescope* (HST; Freedman et al. 1994), assuming the same distance to both galaxies. Observations of the tip of the red giant branch in M82 itself suggest 3.9 ± 0.3 (sys) ± 0.3 (random) Mpc (Sakai & Madore 1999). For consistency with previous work, we adopt the 3.6 Mpc distance, with $1'' = 17$ pc. At this distance a 1 mJy thermal source at 7 mm represents an H II region ionized by the equivalent of ~ 150 O7 stars.

2. OBSERVATIONS

The radio data were acquired with the NRAO VLA⁷ using A- and B-configurations at 43 GHz (NRAO program ID: AT303) and D-configuration at 45 GHz (AM839, PI: D. S. Meier). Weather during the A-array observations in 2004 October was not good enough for useful 7 mm work.

The “high-resolution” (subarcsecond) maps we present in this paper were made in the B-configuration on 2005 April 22 in the continuum observation mode (effective bandwidth ~ 172 MHz). The calibration cycle time for fast switching was set to 100–120 s. 3C147 was used for calibration of the absolute flux scale and 0958+655 was the phase calibrator. Uncertainty in the absolute flux density scale is estimated to be less than 5%, based on VLA estimates of the bootstrap accuracy at 7 mm. For most of our sources, statistical uncertainty due to noise dominates the uncertainty in flux density scale. Total on source time is 1.3 hr. The (u, v) sampling covers 30–1610 $k\lambda$, resulting in a $\sim 0''.2$ beam, the size of which varies slightly with weighting. For our B-array map, the estimated θ_{\max} , the largest angular scale of structures that our observation is sensitive to, is about $3''.5$.

Lower-resolution 7 mm continuum observations (henceforth “low-resolution maps”) were made with the VLA D-array at 45.47 GHz on 2005 November 27 in spectral line mode, as part of a spectral line program (AM839). The setup was two 25 MHz spectrometer tunings per intermediate frequency (IF) set side by side. The UV data set was generated by fitting the UV spectrometer data minus the edge channel with a first-order polynomial using UVLSF task. The net bandwidth is ~ 31 MHz. Because IF 2 has contamination from a recombination line, only IF 1 data is included. The observations used fast-switching with 180 s cycle time. 3C147 and 3C286 were used as flux density calibrators, and 0958+655 was the phase calibrator. Total integration time on source is 2.2 hr. The sampled (u, v) plane covers 5–157 $k\lambda$, resulting in a $\sim 1''.5$ beam. We estimate the θ_{\max} is $\sim 20''$ in our D-array map.

The maps were calibrated and reduced in AIPS following high-frequency reduction procedures, and were deconvolved with CLEAN. The noise level in the maps is ~ 0.1 mJy bm^{-1} for the high-resolution (B-configuration) maps and ~ 0.5 mJy bm^{-1} for the lower-resolution (D-configuration) maps, but varies slightly depending on weighting. Flux measurements and positions were obtained with IMFIT task in AIPS unless otherwise noted. The AIPS task PBCOR was used to correct the flux density scale of these data for the primary beam efficiency of the instrument.

3. OVERVIEW: COMPACT AND DIFFUSE EMISSION SOURCES AT 7 mm IN M82

The high-resolution B-array map (Figure 1(a)) covers the inner $700 \text{ pc} \times 350 \text{ pc}$ ($40'' \times 20''$) of M82 with a $0''.19 \times 0''.15$ (~ 3 pc) beam. Structures larger than $3''.5$ are suppressed in this map. We identify 14 compact sources with flux densities greater than 0.5 mJy ($T_b = 12$ K; 5σ), distributed in a $\sim 40'' \times 10''$ east–west swath with position angle along the optical major axis (Kronberg et al. 1972). The compact sources are high brightness, dense, and luminous H II regions and young SNRs. For the H II regions, our 5σ detection limit corresponds to $N_{\text{Iyc}} \sim 0.6 \times 10^{51} \text{ s}^{-1}$ (assuming optically thin free–free emission), corresponding to about 80 O stars, or a cluster such as R136. The compact optical H II region M82-A1 studied by Smith et al. (2006) falls just below our detection limit.

Properties of the compact sources in natural weighted map are given in Table 1. We adopt the source designations of Kronberg et al. (1985), using the B1950 coordinate of each source relative to $9^{\text{h}}51^{\text{m}} + 69^{\circ}54'$, to facilitate comparisons with earlier studies, but the J2000 coordinates are given also. In Table 2, we have collected the radio continuum flux densities of all 14 compact sources from the literature (18–1.3 cm Unger et al. 1984; Kronberg et al. 1985; Allen & Kronberg 1998; Allen 1999; McDonald et al. 2002) and this work. The flux density measurements at different wavelengths are done at similar resolutions. The beam sizes of maps at 18 cm to 1.3 cm range from $0''.2$ to $0''.3$. The 7 mm measurements quoted in Table 2 (as well as data shown in Figures 2 and 3) are made on a tapered map of $0''.2$ resolution in order to match beam sizes at other wavelengths from the literature. The quoted numbers in Table 2 are total integrated flux densities of compact sources, and the effect of different beams is less than 30%. In Figures 2, 3, and Table 2, we show the SEDs of all 14 compact sources at wavelength 18 cm to 7 mm. The details of model fitting are included in Table 3. Our discussion of properties of these compact sources, including their SEDs, can be found in Sections 4.1 and 6.

The high-resolution B-array map also reveals four regions of comparatively extended emission ($EM = \int n_e^2 dl$). The bright, high-frequency free–free emission detected here arises from gas with very high emission measure, so it is surprising to find such extended sources. They are $1''$ – $2''$ across, or 17–35 pc. They are similar in extent to the large H II region associated with NGC 3603 in our Galaxy, but with a much higher brightness and EM. We discuss the significance of these high brightness, extended regions in Section 4.3.

The low-resolution D-array map is shown in Figure 1(b). This map, with a beam of $1''.99 \times 1''.47$ P.A. 17° , is sensitive to lower brightness emission, $T_b \sim 0.1$ K rms ($\sigma \sim 0.5$ mJy bm^{-1}) and also more extended emission structures (up to $60''$, covering the entire field shown) than the high-resolution map. The low-resolution image shows four major peaks with intensity 12 mJy bm^{-1} or higher. The integrated flux density in the naturally weighted D-array map is 1.2 ± 0.1 Jy. The total flux reported for M82 from WMAP at 41 GHz flux density is 1.3 ± 0.2 Jy (Bennett et al. 2003). Thus our low-resolution D array map recovers, within the uncertainties, all the 7 mm flux density. The diffuse emission structure is elongated in the same direction and over the same extent as the swath of compact sources, and agrees with the orientation of the stellar elliptical component seen in the deep near infrared images (Mayya et al. 2005).

⁷ The National Radio Astronomy Observatory is a facility of the *National Science Foundation* operated under cooperative agreement by Associated Universities, Inc.

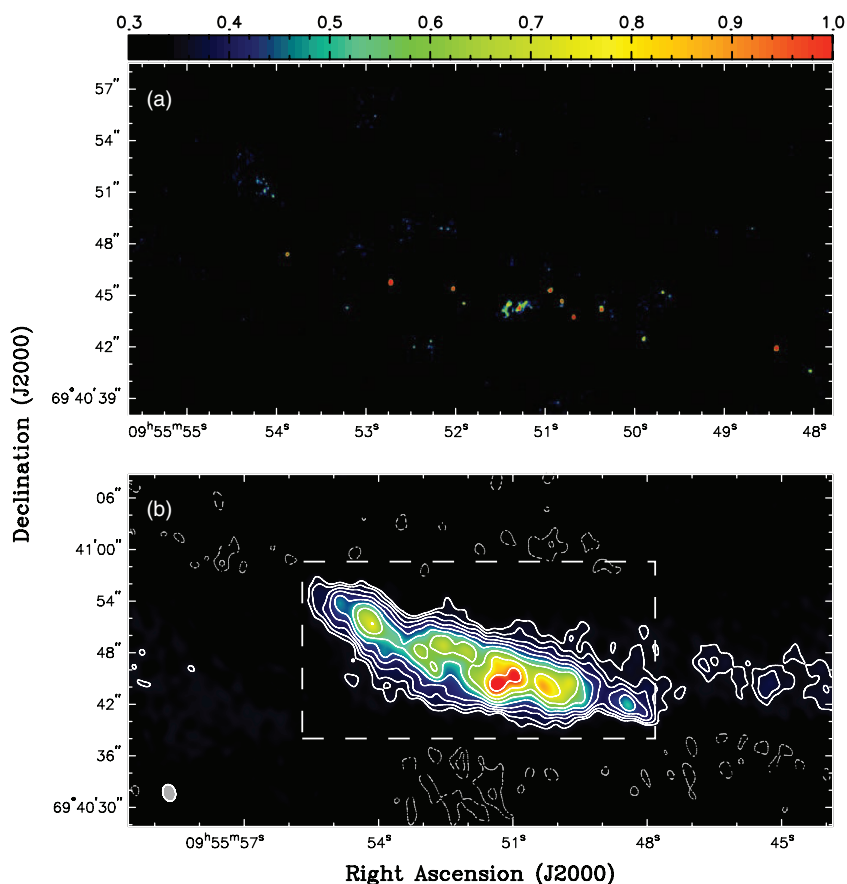


Figure 1. M82 radio continuum maps at 7 mm. (a) Naturally weighted map from the VLA B-configuration data. The color scheme is indicated by the color wedge on the top, with flux density values in mJy beam^{-1} . The synthesized beam is $0''.19 \times 0''.15$, P.A. = -10° . This map is sensitive to structures up to $\theta_{\text{max}} \sim 3''.5$. The peak flux is $5.2 \text{ mJy beam}^{-1}$. (b) Robustly weighted map made from the D-configuration data. Synthesized beam is $1''.99 \times 1''.47$, P.A. = 17° beam. The θ_{max} is $\sim 20''$. Contours are half-integral powers of $2 \times 1.12 \text{ mJy beam}^{-1}$. The dashed box shows the region displayed in (a).

Table 1
Compact 7 mm Continuum Sources: Positions and Fluxes

Source ^a (B1950)	Other Name ^b (A99/M02)	α (J2000) ^c 09 ^h 55 ^m + (°)	δ (J2000) ^c 69°40'+ (")	$S_{7\text{mm}}^{\text{Peak}}$ ^d (mJy beam^{-1})	$S_{7\text{mm}}$ ^d (mJy)	Size ^e " × " , °
39.277+54.32	39.29+54.2	48.051	40.64	0.9	1.4 ± 0.4	0.31, 0.25, 60
39.659+55.73	39.68+55.6	48.427	41.97	3.6	4.6 ± 0.3	0.21, 0.18, 170
40.933+58.98	40.94+58.8	49.694	45.20	0.6	2.3 ± 0.6	0.47, 0.35, 70
41.145+56.29	41.17+56.2	49.904	42.51	0.8	3.1 ± 0.6	0.38, 0.30, 170
41.628+58.01	41.64+58.4	50.375	44.22	1.2	3.5 ± 0.5	0.33, 0.26, 0
41.942+57.62	41.95+57.5	50.686	43.77	2.6	2.1 ± 0.2	0.18, 0.13, 180
42.072+58.52	42.58+58.4	50.817	44.69	1.2	2.2 ± 0.3	0.28, 0.19, 10
42.193+59.13	42.21+59.2	50.945	45.32	1.4	2.6 ± 0.3	0.26, 0.21, 130
42.549+58.13	42.56+58.0	51.291	44.29	0.9	9.2 ± 1.3	0.68, 0.44, 140 ^f
42.673+58.32	42.69+58.2	51.414	44.47	0.6	9.3 ± 1.5	0.82, 0.52, 140 ^f
43.173+58.43	43.18+58.3	51.908	44.56	0.7	1.2 ± 0.3	0.25, 0.19, 90
43.295+59.27	43.31+59.2	52.028	45.42	1.6	2.0 ± 0.3	0.22, 0.17, 170
43.992+59.70	44.01+59.6	52.723	45.78	5.2	5.4 ± 0.2	0.20, 0.16, 180
45.153+61.34	45.17+61.2	53.875	47.41	1.1	1.9 ± 0.3	0.23, 0.21, 170

Notes.

^a Convention of Kronberg et al. (1985).

^b A99: Allen (1999) and M02: McDonald et al. (2002).

^c The typical uncertainty of position within the 7 mm map is ~ 10 – 20 mas for strong sources, and 30 – 40 mas for weaker sources (flux density $\lesssim 1 \text{ mJy beam}^{-1}$). The absolute astrometry accuracy is estimated to be $\sim 0''.1$, limited by the atmospheric phase stability during the observation.

^d $S_{7\text{mm}}^{\text{Peak}}$ and $S_{7\text{mm}}$: peak flux density and total integrated flux density of 7 mm continuum, respectively, with beam as $0''.19 \times 0''.15$, P.A. = -10° . The rms uncertainty of each measurement is $0.13 \text{ mJy beam}^{-1}$. The systematic error of flux density is expected to be $\lesssim 5\%$.

^e Convolved size. Single Gaussian is assumed for each source; using AIPS task IMFIT. The typical uncertainty of source size (convolved) is $\lesssim 10\%$ except source 42.69+58.2 and 42.56+58.0 in which the uncertainty is $\sim 20\%$.

^f Peaks in emission complex.

Table 2
Radio SEDs of Compact Sources

Source ^a (B1950)	$S_{18\text{cm}}^b$ (mJy)	$S_{6\text{cm}}^b$ (mJy)	$S_{3.6\text{cm}}^b$ (mJy)	$S_{2\text{cm}}^b$ (mJy)	$S_{1.3\text{cm}}^b$ (mJy)	$S_{7\text{mm}}^b$ (mJy)	Reference ^c
39.277+54.32	...	1.7 ± 0.2	...	1.5 ± 0.2	...	1.5 ± 0.5	M02
39.659+55.73	...	1.5 ± 0.2	...	3.2 ± 0.2	...	8.0 ± 0.6	M02
40.933+58.98	...	1.9 ± 0.2	2.9 ± 0.1	2.8 ± 0.3	2.2 ± 0.3	2.5 ± 0.4	A99
41.145+56.29	...	2.0 ± 0.3	...	2.8 ± 0.2	...	5.1 ± 0.6	M02
41.628+58.01	...	1.0 ± 0.2	...	1.8 ± 0.2	...	6.1 ± 0.5	M02
41.942+57.62 ^d	79.0 ± 4.0	40.0 ± 0.9	26.8 ± 0.5	17.9 ± 1.7	12.0 ± 0.6	2.4 ± 0.3	AK98
42.072+58.52	...	1.2 ± 0.4	...	1.7 ± 0.2	...	3.6 ± 0.6	M02
42.193+59.13	2.5 ± 1.0	4.1 ± 0.5	4.3 ± 0.3	4.5 ± 0.3	4.1 ± 0.3	4.0 ± 0.5	AK98
42.549+58.13	...	2.7 ± 0.4	...	1.8 ± 0.2	...	1.7 ± 0.2 ^e	M02
42.673+58.32	...	1.0 ± 0.4	...	1.8 ± 0.2	...	1.1 ± 0.2 ^e	M02
43.173+58.43	8.5 ± 1.0	5.2 ± 0.2	3.8 ± 0.2	2.4 ± 0.3	1.8 ± 0.3	1.6 ± 0.5	AK98
43.295+59.27	19.5 ± 1.0	10.3 ± 0.2	8.0 ± 0.1	5.5 ± 0.3	4.1 ± 0.4	2.5 ± 0.5	AK98
43.992+59.70	9.5 ± 1.0	21.8 ± 0.9	20.2 ± 0.1	15.8 ± 0.3	12.5 ± 0.3	5.4 ± 0.4	AK98
45.153+61.34	12.5 ± 1.0	7.9 ± 0.3	5.7 ± 0.1	3.9 ± 0.3	2.5 ± 0.3	2.2 ± 0.5	AK98

Notes.

^a Convention of Kronberg et al. (1985)

^b S_λ : Total integrated flux density of radio continuum at wavelength λ with $0''.2$ to $0''.3$ beam. See Section 3 for details.

^c The flux densities at 18–1.3 cm are adopted from AK98: Allen & Kronberg (1998; and references therein); A99: Allen (1999); M02: McDonald et al. (2002).

^d The source is a known strong variable. The flux density densities measured at different epochs have been corrected to the epoch of 1993.4 using a decline rate of 8.8% (see Allen & Kronberg 1998, for details), except 7 mm flux density, which is measured in 2005 in this work.

^e Source is in emission complex. The peak flux density at 7 mm obtained with IMFIT is used. This could be an underestimate if the source is resolved.

We have fitted 17 peaks in the low-resolution map with Gaussians, and the corresponding flux densities, locations, and the sizes of the peaks are listed in Table 4. All these peaks are found in the longer wavelength VLA images of Allen (1999) except peaks W4a and E1a, which are newly identified in this work. The peaks sum to ~ 0.65 Jy at 7 mm. If this flux density associated with low-resolution peaks is all optically thin free-free emission, and $T_e = 10,000$ K, the inferred Lyman continuum photon rate (N_{lyc}) is $\sim 8.4 \times 10^{53} \text{ s}^{-1}$. (For T_e of 5000 K, N_{lyc} would increase by 30%–40%.) This value is in good agreement with that estimated from the free-free continuum at longer wavelengths by Allen (1999, $9.1 \times 10^{53} \text{ s}^{-1}$, from 1.3–20 cm multiwavelength spectral decomposition modeling), and at shorter wavelengths by Carlstrom & Kronberg (1991) and Matsushita et al. (2005), who find $6.9 \times 10^{53} \text{ s}^{-1}$ and $7.9 \times 10^{53} \text{ s}^{-1}$ at 3 mm and 2.6 mm, respectively (these numbers are interferometric and therefore are lower limits). It also agrees with that suggested from recombination line studies (Seaquist et al. 1985) and the extinction-corrected MIR fluxes of Förster Schreiber et al. (2001). The good agreement in N_{lyc} between our analysis and previous studies indicates that the peaks we see in the low-resolution map of Figure 1(b) dominate the total free-free emission.

Nonthermal emission at 43 GHz is weak, but contributes a non-negligible fraction of the integrated flux density in M82. The estimate of the nonthermal component is 35% of the total at 7 mm, extrapolating from VLA cm-wave flux densities of the same region (Allen 1999). This would give a thermal flux density of ~ 0.8 Jy, 15%–20% higher than 0.65 Jy we obtain from summing the peaks in the D-array map of Figure 1(b). We attribute the discrepancy to thermal emission from some H II regions distributed on too large a spatial scale to be seen in peaks in these images.

4. STAR FORMATION TRACER: 7 mm CONTINUUM EMISSION IN M82

4.1. The Compact Thermal Radio Sources

The 14 compact sources of the high-resolution map (Figure 1(a)) contribute $\lesssim 10\%$ of the total 7 mm flux density in the low-resolution D-array map (Figure 1(b)). These compact sources in the 7 mm high-resolution B-array map also appear in lower-frequency radio continuum maps (Muxlow et al. 1994; Huang et al. 1994; Wills et al. 1997; Allen & Kronberg 1998; Allen 1999; McDonald et al. 2001; Fenech et al. 2008). We have computed radio SEDs for the 14 sources, which are shown in Figures 2 and 3, with details of the SED modeling given in Table 3. We identify nine regions with spectral index $\alpha \gtrsim -0.2$ ($S \propto \nu^\alpha$) as H II regions, and the others as SNRs. The flux densities at 43 GHz and the spectral indices are consistent with previous SEDs and source characterizations (Allen & Kronberg 1998; McDonald et al. 2002) except for the two nonthermal sources 43.992+59.70 and 41.942+57.62, which are discussed in Sections 6.1 and 6.3, respectively.

Of the nine H II regions in the high-resolution map, two have flux densities at more than five frequencies. Fitting of the spectra of these two sources suggests that they have free-free turnover frequencies (where $\tau \sim 1$) $\nu_t \sim 2.5$ –5 GHz. To have $\nu_t \sim$ a few GHz requires emission measures of 2 – $9 \times 10^7 \text{ pc cm}^{-6}$.

The other sources have flux densities at only three frequencies, and a single power law represents their observed flux densities fairly well (Figure 2). Some of the deviations may be due to small amounts of extended emission in the sources and the slightly (15%–20%) differing beams of the flux densities from the literature. Four sources have rising SED ($\alpha > 0$). Rising spectrum radio sources have been found in many extragalactic systems, and are thought to be giant compact H II

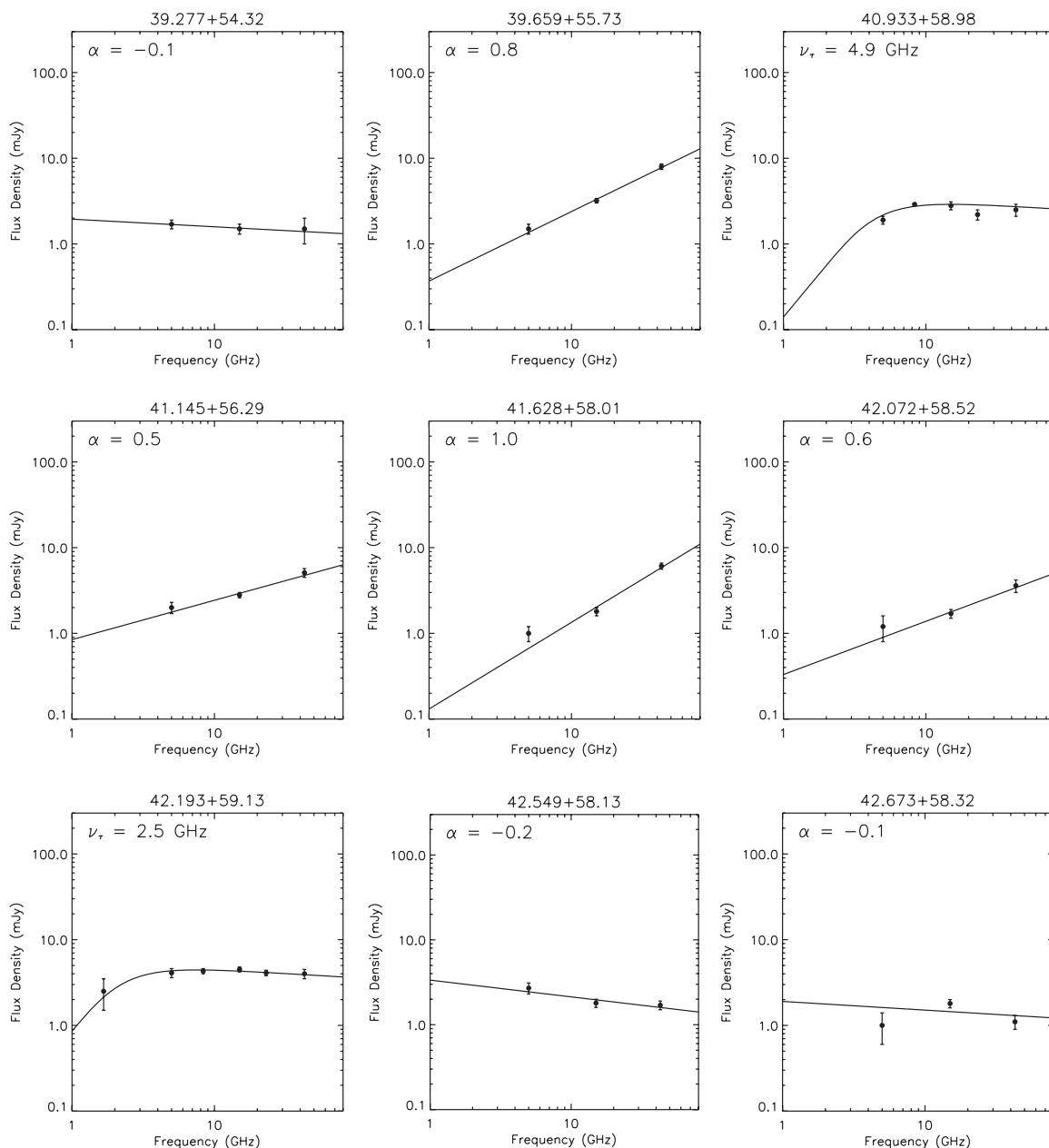


Figure 2. SED of nine thermal sources found in 7 mm high-resolution ($\theta/2$) map. The line represents the best-fit single power-law SED except in the cases of 40.933+58.98 and 42.193+59.13 where the line indicates free–free self-absorption.

regions with high electron density (Turner et al. 1998). These are much larger than Galactic compact H II regions because the super star clusters (SSCs), the clusters exciting them, are much larger both in excitation and in physical size. For the sources here, the emission appears to remain partially optically thick at frequencies up to 43 GHz, so we expect to see brightness temperatures of 10^2 – 10^3 K. Their observed brightness temperatures are lower than this, and imply EMs $\gtrsim 3.5 \times 10^7$ pc cm $^{-6}$ (derived from peak flux density), consistent with turnover frequencies of 3 GHz, an order of magnitude lower than observed. The low brightness temperatures indicate small filling factors, and signal the presence of very compact sources of significantly less than 3 pc extent, which we cannot resolve.

Considering the radio continuum luminosity, brightness of the emission, and the turnover frequency, these appear to be

young H II regions, and we infer that the star clusters exciting these nebulae are also relatively young. The total flux density of just the detected compact H II regions comes to ~ 38 mJy, which is $\sim 6\%$ of the total thermal flux density at 7 mm (at the same sensitivity), in other words, $\sim 6\%$ of the ionizing flux density. But the high-resolution 7 mm image fails to detect all of the compact H II regions in M82, even fairly optically luminous ones such as M82-A1 (Smith & Gallagher 2001), so we believe that there are more compact regions below our current detection limit. In this case the H II region phase in M82 must last at least $\sim 6\%$ of the ~ 10 Myr lifetime of O stars, and possibly longer, to a Myr or more. To restrain the H II regions from expanding requires external or internal confinements, perhaps external high pressures (de Pree et al. 1995; Smith et al. 2006), or in the larger clusters, potentially slowing by gravity (Turner et al. 2003).

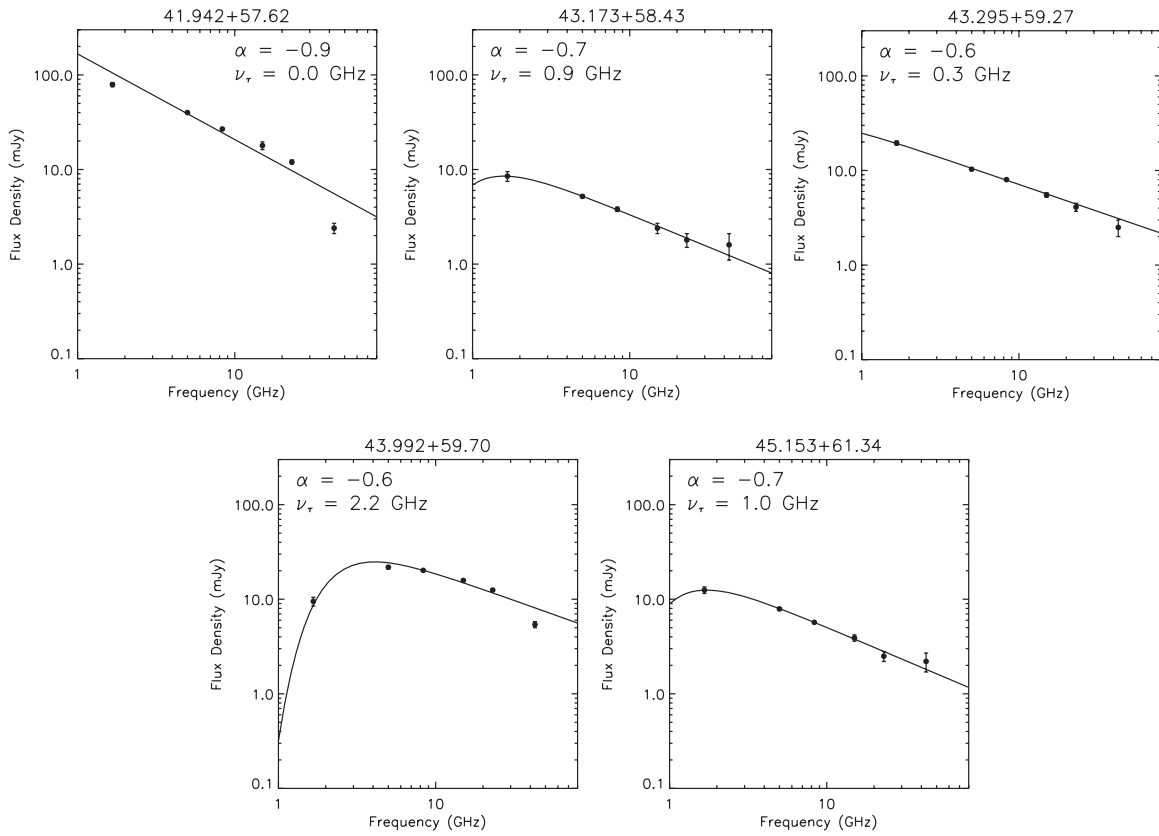


Figure 3. SED of five nonthermal sources found in 7 mm continuum high-resolution ($0''.2$) map. Line represents power-law synchrotron radiation with free-free absorption.

Table 3
SED Models of Compact Sources

Source (B1950)	Type ^a	Model ^b	α^c	$\nu_{\tau=1}^c$ (GHz)	EM ^d (10^6 pc cm ⁻⁶)	N_{lyc}^e 10^{50} s ⁻¹	N_O	L_{OB} $10^8 L_{\odot}$
39.277+54.32	H II	PL	-0.1	< 5	< 90	22	220	0.4
39.659+55.73	H II	PL	0.8	> 43	> 8000	116	1160	2.3
40.933+58.98	H II	FFSA	...	4.9	85	36	360	0.7
41.145+56.29	H II	PL	0.5	> 43	> 8000	74	740	1.5
41.628+58.01	H II	PL	1.0	> 43	> 8000	88	880	1.8
42.072+58.52	H II	PL	0.6	> 43	> 8000	52	520	1.0
42.193+59.13	H II	FFSA	...	2.5	20	58	580	1.2
42.549+58.13	H II	PL	-0.2	< 5	< 90	25	250	0.5
42.673+58.32	H II	PL	-0.1	< 5	< 90	16	160	0.3
41.942+57.62 ^f	SNR	PL+FFA	-0.7/ -0.9 ^f
43.173+58.43	SNR	PL+FFA	-0.7	0.9	2.7
43.295+59.27	SNR	PL+FFA	-0.6
43.992+59.70	SNR	PL+FFA	-0.6	2.2	6.6
45.153+61.34	SNR	PL+FFA	-0.7	1.0	3.0

Notes.

^a Based on the previous cm results from Allen & Kronberg (1998); Allen (1999); McDonald et al. (2002).

^b PL: single power law; FFSA: free-free emission with self-absorption; FFA: foreground free-free absorption.

^c α : spectral index, $S_{\nu} \propto \nu^{\alpha}$. ν_{τ} : turnover frequency.

^d $EM \propto (\nu_{\tau=1})^2$. $T_e = 10,000$ K is assumed.

^e Assuming optically thin free-free emission. For optically thick sources, the numbers would be the lower limits.

^f Variable source. $\alpha = -0.7$: with epoch corrected (1993.4) data at wavelengths at 18–1.3 cm. $\alpha = -0.9$: with all radio continuum data, including flux density at 7 mm of epoch 2005. See Section 6.3.

4.2. Lack of Optical/Near-IR Continuum Counterparts

The compact sources are shown in Figure 4 overlaid on a color (VRI) image from the *Spitzer* Legacy project SINGS (Kennicutt et al. 2003). Nearly all of the compact sources are found in

dust lanes. The only exception is source 43.922+59.70, which is located near the dynamical center, and a potential active galactic nucleus (AGN) candidate (Section 6.)

We have attempted to align the compact radio sources identified in this and previous work (Allen 1999; McDonald

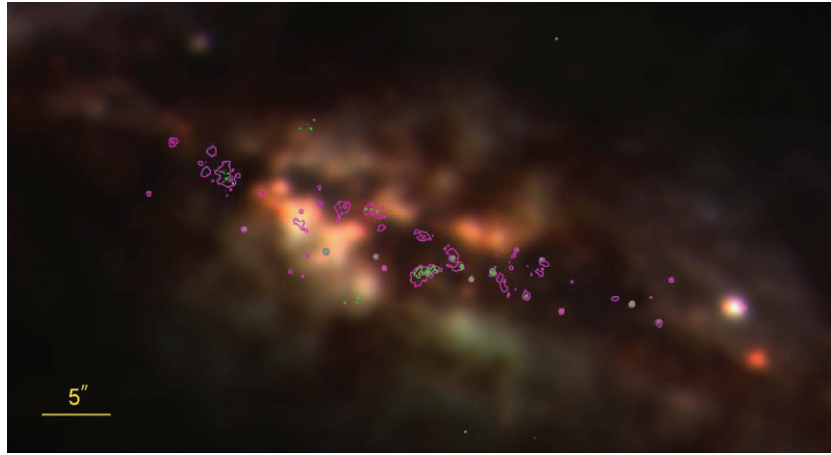


Figure 4. Compact radio sources overlaid on false color VRI image from *Spitzer* SINGS project. The magenta contours at integers $\times 0.5$ mJy beam $^{-1}$ show 2 cm emission reproduced from VLA archive data (AM671; McDonald et al. 2002) at resolution $\sim 0''.2$. The green contours at integers $\times 0.8$ mJy beam $^{-1}$ present the 7 mm sources shown in Figure 1(a).

et al. 2002, and references therein) with the published *HST* NIR continuum images of Alonso-Herrero et al. (2003) and McCrady et al. (2003), the cataloged optical clusters (Melo et al. 2005), and the archived *HST* optical measurements. There is no consistent alignment of the radio and other sources within the *HST* pointing uncertainty. The H II regions we see are presumably associated with young SSCs; that the clusters are not seen in the optical/near-IR continuum argues that the extinction must be high ($A_K > 6$). The molecular clouds alone can contribute A_V of 10^2 – 10^3 if they happen to be along the line of sight to the H II regions.

If the average extinction at arcsecond resolution is $A_V \sim 14$ (from $H-K$ color by McLeod et al. 1993, assuming $A_V/A_K = 10$), the line-of-sight extinctions implied in the lack of NIR sources to these young clusters must be 4 times higher. This is consistent with the high average ($A_K \gtrsim 1$) and patchy extinction derived on large ($11''$, or ~ 200 pc) scales toward the H II regions in M82 from Brackett line observations by Willner et al. (1977, $A_V = 25$), Simon et al. (1979, $A_V = 14$), Rieke et al. (1980, $A_V = 26$), and Förster Schreiber et al. (2001, $A_V \sim 50$), much of which appears to be internal to the H II regions themselves.

In the $Pa\alpha$ image of Alonso-Herrero et al. (2003), we identify three (39.227+54.32, 40.933+58.98, and 42.072+58.52) out of our nine compact thermal sources, and one nonthermal source (43.992+59.70) as associated with compact $Pa\alpha$ structures. If the $Pa\alpha$ emission is associated with the corresponding radio H II regions, we estimate, based on the inferred Lyman continuum flux densities, that the extinction toward these IR-visible nebulae is $A_K \gtrsim 9$. None of these three sources are apparent in the *HST* NIR continuum images, and it agrees with the high extinction suggested in the $Pa\alpha$ image.

4.3. High EM Extended Structures at 7 mm: Sheets of Hot Gas

Besides the compact dense sources in Table 3, we detect extended regions in M82 with relatively high EM. In Figure 5, we show B-array maps of free-free emission regions with integrated flux density of 50–70 mJy in $5''$ – $9''$ area. These regions have $EM = 1.2$ – 2.0×10^7 pc cm $^{-6}$. This agrees with the D-array measurements shown in Table 4.

High EM can be produced either by high rms electron density or by a long sightline (dl) of ionized gas. If high electron density

is responsible, then to reconcile the high EM with the observed flux (N_{lyc}) requires that the line-of-sight length be much smaller than the observed transverse distance. For example, to maintain the ionization of a spherical volume of radius 15 pc, the observed transverse diameter of source in Figure 5(a), and rms electron density 10^3 cm $^{-3}$ ($\gtrsim 5 \times 10^3$ cm $^{-3}$ was inferred by Rodriguez-Rico et al. 2004 in a $2''$ resolution) requires a Lyman continuum rate of $N_{\text{lyc}} \sim 2 \times 10^{53}$ s $^{-1}$. The observed flux of this structure indicates $N_{\text{lyc}} \sim 10^{52}$ s $^{-1}$. This implies that the actual emitting volume is smaller, i.e., the emitting region is sheet-like. There are a number of such patches evident in Figure 5. While these large regions of high electron density are dynamically stable in the high pressure $P/k \gtrsim 10^7$ cm $^{-3}$ K environment of the M82 starburst, the excitation requirements are inconsistent with other star formation indicators, with the possible exception of the “yin-yang” shaped source (Figure 5(c)) located at the peak of the low-resolution map (Figure 1). These structures could be the ionized surfaces of chimneys (Wills et al. 1999b) or superbubbles (Neininger et al. 1998; Weiß et al. 1999; Wills et al. 1999b; Matsushita et al. 2000, 2005). The coincidence of their locations with dust lane and CO gas distribution implies that they are associated with in the molecular clouds, which would be consistent with an origin in the outer, ionized layers of large molecular clouds.

Despite its location near the edge of the superbubble, the “yin-yang” source is an exception in that it does appear to have sufficient flux to support the ionization, and there is a bright MIR source here too (Achtermann & Lacy 1995; Lipsy & Plavchan 2004). However, this source has an unusual structure that is coherent and bubblelike on a scale of $1''.5 = 26$ pc. If this were a bubble, an energy of $10^{50.5}$ erg would be required to clear the inner region of gas.

Another explanation for these extended regions is that they represent a collection of smaller H II regions representing distributed star formation at the end of the stellar bar in M82. Regions (b)–(d) in Figure 5 are distributed on the $10''$ ionized ring of M82 (Larkin et al. 1994; Achtermann & Lacy 1995), which may represent the x_2 -orbits of a bar (Telesco et al. 1991; Larkin et al. 1994; Achtermann & Lacy 1995; Greve et al. 2002). The region (a) is on the east ionized ridge, and probably near the end of the x_2 -orbits. Star formation is observed to be near bar ends, perhaps facilitated by cloud–cloud collisions.

Table 4
Properties of Peaks in Low-Resolution Map

Region ^a	Peak Position ^b (J2000) (09 ^h 55 ^m +; 69°40'+)	$S_{7\text{cm}}^c$		EM ^d (10^6 pc cm^{-6})	N_{lyc}			N_{07}^d ($\times 100$)	L_{OB}^d ($10^8 L_{\odot}$)	L_{MIR}^f ($10^8 L_{\odot}$)
		Peak (mJy bm^{-1})	Total (mJy)		(7 mm ^d) (10^{52} s^{-1})	(100 GHz ^e) (10^{52} s^{-1})	(MIR ^f) (10^{52} s^{-1})			
W1	48.08, 40.8	2.4	4	16.0	0.6	6	1.2	...
W2	48.44, 42.0	4.1	8	10.5	1.2	12	2.3	...
W3	49.77, 44.3	8.2	39	12.5	5.7	...	0.08	57	11	0.2
W4	49.96, 42.9	8.1	38	12.9	5.5	2.8	...	55	11	...
W4a	49.50, 42.3	4.6	19	7.4	2.8	28	5.5	...
W5	50.29, 44.1	11	65	15.5	9.4	3.6	2.4	94	19	5.9
R1	50.98, 45.2	13	81	18.5	11.8	3.8	2.2	118	24	5.5
R2	51.33, 44.4	15	82	22.3	11.9	4.2	1.3	119	24	3.3
R3	51.30, 46.2	9.5	65	13.0	9.4	94	19	...
R4	52.06, 48.1	6.9	41	10.4	6.0	2.3	0.7	60	12	1.7
R5	52.55, 48.8	7.3	40	10.6	5.8	...	0.9	58	12	2.3
R6	52.77, 46.2	6.0	23	9.5	3.3	33	6.7	...
R7	53.06, 48.1	5.9	39	8.4	5.7	2.2	2.0	57	11	4.9
E1	53.66, 49.7	4.3	29	6.1	4.2	42	8.4	...
E1a	53.86, 48.1	3.4	10	6.4	1.5	15	2.9	...
E2	54.00, 51.4	8.1	54	11.5	7.8	2.4	...	78	16	...
E3	54.82, 53.4	2.7	16	3.8	2.3	23	4.6	...

Notes.

^a Following the name in Allen (1999) except W4a and E1a which are newly identified in this work.

^b Typical peak position uncertainty is $\sim 0.''1-0.''2$.

^c In robust weighted, VLA D-array map at 45 GHz with $1.''6 \times 1.''2$, P.A. = 20° beam, rms = 0.3 mJy bm^{-1} ; using IMFIT task in AIPS

^d Assume $T_e = 10,000$ K, and pure optically thin thermal emission at 7 mm. The possible nonthermal contamination is estimated to be $\lesssim 35\%$.

^e Adopted from Matsushita et al. (2005). Derived from peak flux density at 100 GHz with $2.''3 \times 1.''9$ beam. Assume $T_e = 10,000$ K.

^f Adopted from Lipsy & Plavchan (2004). Their seeing-limited MIR images are in $0.''4-1.''0$ resolution.

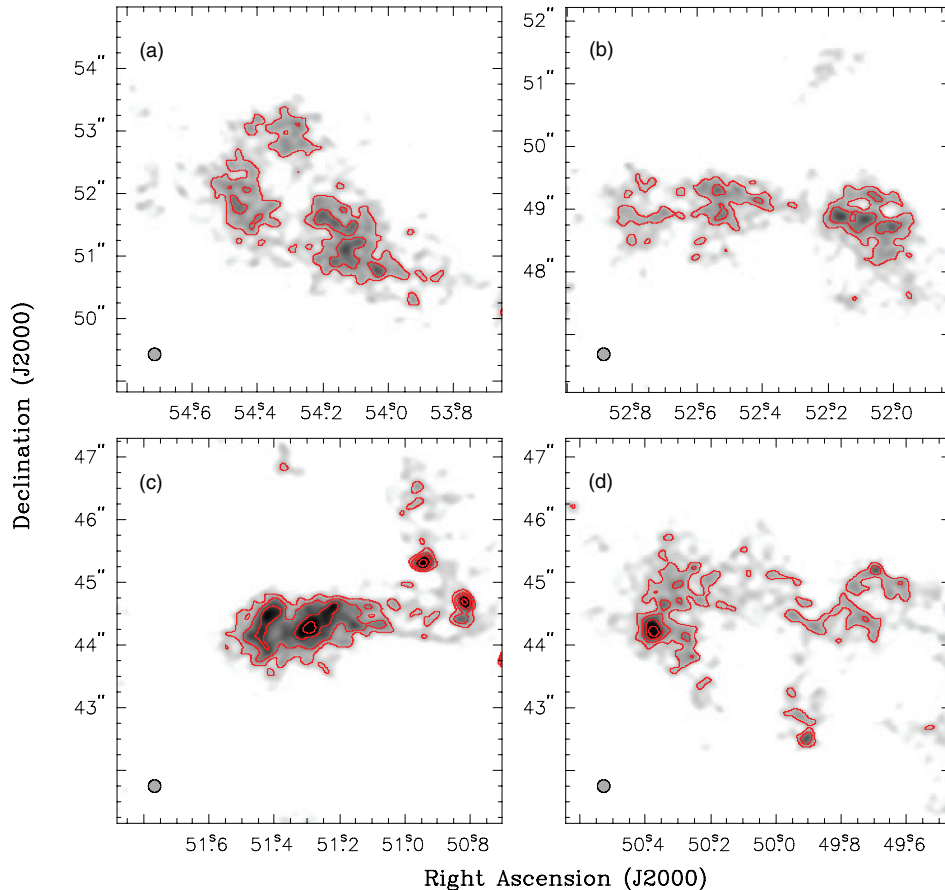


Figure 5. 7 mm continuum emission from extended sources in M82 at 09^h55^m; +69°40'. The contours are $2^{\frac{n}{2}} \times 0.6 \text{ mJy } \text{bm}^{-1}$ in integer n . Maps are generated with (u, v) restriction of $30-1600 \text{ k}\lambda$ in $0.''2 \times 0.''2$ beam.

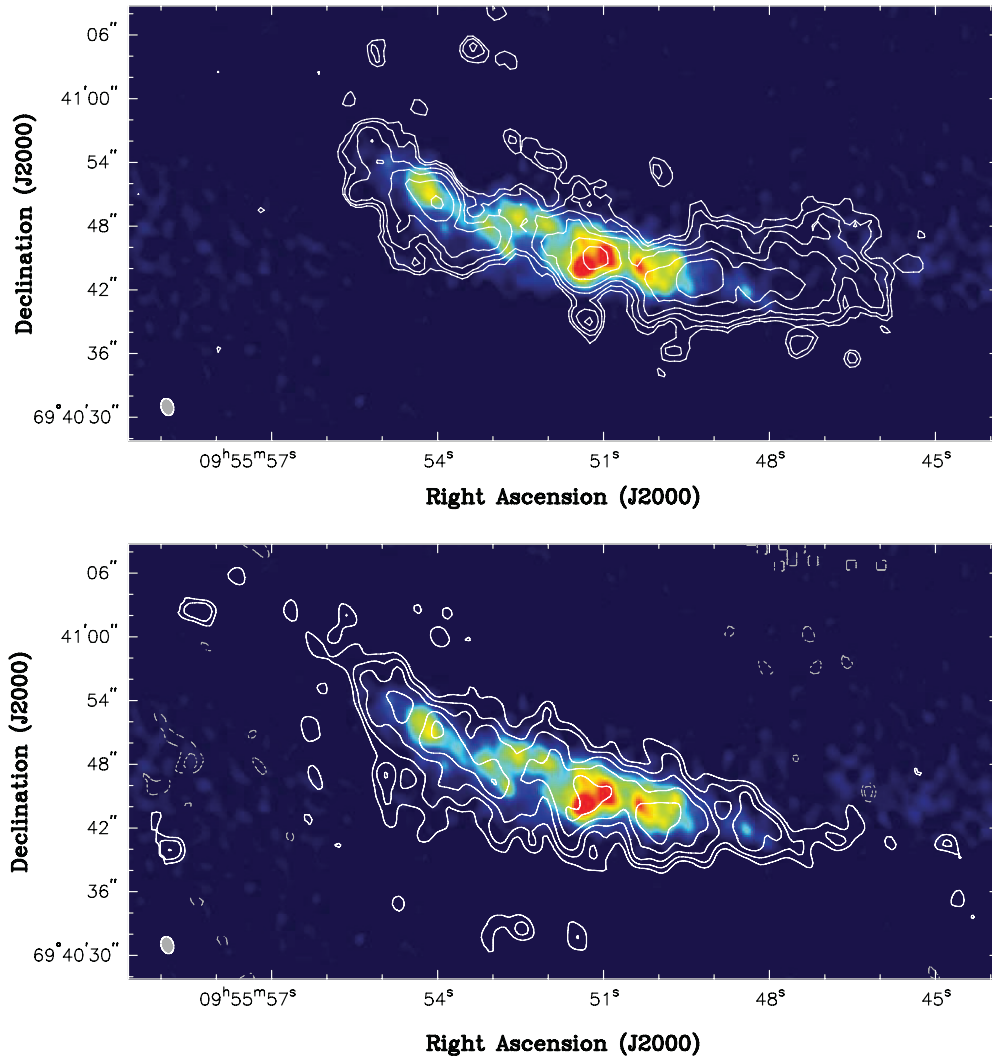


Figure 6. Molecular line emission contours overlaid on color images of the D-array 7 mm continuum robust ($R = 0$) map. The contours on the top are CO(1-0) from Shen & Lo (1995). The contours are $2\frac{1}{2} \times 5 \text{ Jy bm}^{-1} \text{ km s}^{-1}$. On the bottom is the HCN from Schilke (private communication). The contours are $2\frac{1}{2} \times 0.8 \text{ Jy bm}^{-1} \text{ km s}^{-1}$.

4.4. H II Regions, Molecular Gas, and Dust

4.4.1. Correlation with Molecular Gas: CO(1-0) and HCN(1-0) Line Emission

The dense star-forming regions traced by high brightness 7 mm free-free emission are likely to be still close to their natal giant molecular clouds (GMCs). We therefore expect high correlation of thermal free-free emission and molecular line emission, although at some sufficiently high resolution, they should begin to anticorrelate. In Figure 6, we show the 7 mm map with contours of CO(1-0) line emission from the OVRO map of Shen & Lo (1995) and an HCN(1-0) map from the Plateau de Bure Interferometer (Schilke, private communication). The molecular gas tracer CO(1-0) is more extended in the plane of the galaxy, while the dense molecular gas tracer HCN(1-0) emission is confined to the star formation area. It is apparent that the correlation of the 7 mm continuum emission, largely free-free emission, with HCN gas is excellent.

A quantitative comparison of the molecular line fluxes and the free-free flux confirms this conclusion. Figure 7 shows the beam-to-beam comparison between the low-resolution

7 mm emission and HCN. The linear correlation between HCN and radio continuum shown in Figure 7 agrees with the tight correlation between global HCN emission and star formation tracers (such as far-infrared emission) discovered in local normal spiral and starburst galaxies Gao & Solomon (2004a), in Galactic molecular dense cores (Wu et al. 2005), and in high-redshift galaxies (Gao et al. 2007). Our plot shows that this good correlation between dense molecular gas and star formation extends down to scales of tens of pc.

To more directly compare our results with Gao et al. (2007) who determined the correlation in terms of infrared luminosity, L_{IR} and HCN line flux, we have translated the 7 mm flux density into L_{IR} . We assume an O-star-dominated stellar population which yields the relation of $L_{\text{IR}} \sim L_{\text{OB}} \sim 2 \times 10^5 L_{\odot} \times (\frac{N_{\text{Iyc}}}{10^{49} \text{ s}^{-1}})$, following Turner et al. (2000) and Beck et al. (2002), or $L_{\text{IR}} \sim 2.9 \times 10^7 L_{\odot} \times (\frac{S_{7\text{mm}}}{\text{mJy}})$ at 3.6 Mpc. This relation could result in underestimates if evolved stellar populations contribute significantly to L_{IR} . Our 7 mm values are plotted with the data of Gao et al. (2007) on Figure 8. Further discussion of this correlation is in Section 5.2.

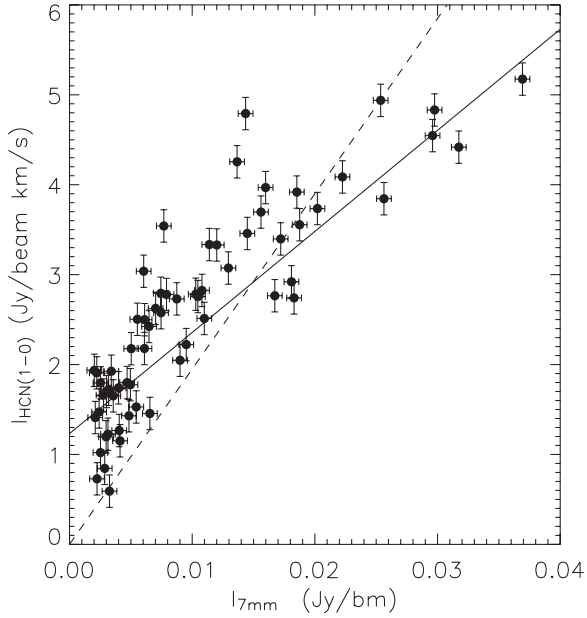


Figure 7. Intensity of HCN ($J = 1 - 0$) line vs. D-array radio continuum strength at 7 mm. Each point on the plot represents independent measurements with a $2''.7 \times 2''.7$ beam for flux density greater than 3σ . The solid and dashed lines represent the linear regression result of $I_{\text{HCN}} \sim 112I_{7\text{mm}} + 1.2$ and $I_{\text{HCN}} \sim 195I_{7\text{mm}}$ (forced zero intercept), respectively.

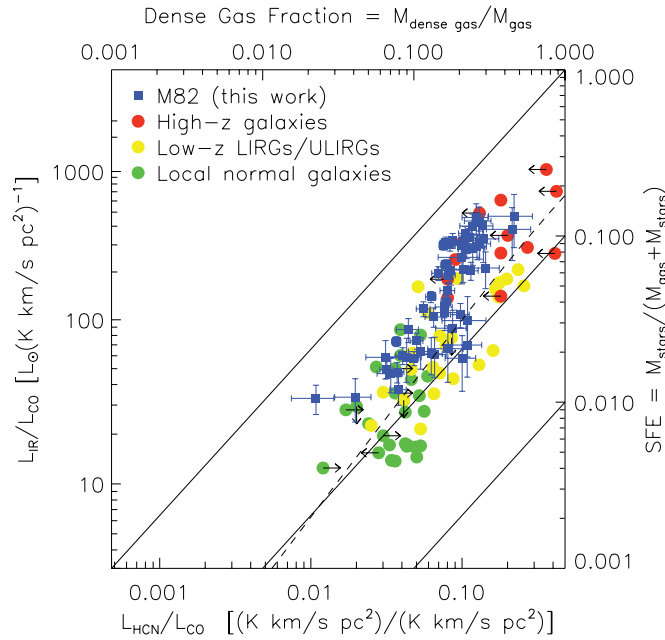


Figure 8. Correlation between $L_{\text{IR}}/L_{\text{CO}}$ and $L_{\text{HCN}}/L_{\text{CO}}$. The filled blue squares are data of M82 at $2''.7$ resolution. Data points of M82 with less than 3σ detection are suppressed. Green ($L_{\text{IR}} < 10^{12} L_{\odot}$) and yellow dots ($L_{\text{IR}} \geq 10^{12} L_{\odot}$, LIRGs or ULIRGs) are galaxies in local universe while the red dots are high-redshift galaxies (Gao et al. 2007). We estimate L_{IR} from the total 7 mm flux density by assuming the $L_{\text{IR}} = L_{\text{OB}}$ is dominated by the ZAMS population that excite the 7 mm H II regions (see the text for details). The dashed line represents the correlation found by Gao & Solomon (2004a). The axes on the top and right show the corresponding dense gas fraction (DGF) and star formation efficiency (SFE). The solid diagonal lines from the top to the bottom represent the ratio between SFE and DGF as 1, 0.1, and 0.01, respectively.

4.4.2. Correlation with Spitzer $8 \mu\text{m}$ Emission

The polycyclic aromatic hydrocarbon (PAH) emission features in the MIR are expected to trace photodissociation regions

(PDRs) generated by the softer UV photons produced by OB stars (Hollenbach & Tielens 1997). Emission in the $8 \mu\text{m}$ band of the IRAC camera is dominated by aromatic feature emission (Engelbracht et al. 2006), probably PAHs. The contribution of starlight to the $8 \mu\text{m}$ band is estimated to be minimal, at $\sim 10\%$ (based on IRAC $3.6 \mu\text{m}$ flux; Helou et al. 2004). The resolution of IRAC at this wavelength, $1''.7$, is comparable to our low-resolution 7 mm image.

M82 was observed at $8 \mu\text{m}$ by IRAC on *Spitzer* as part of the *Spitzer* Infrared Nearby Galaxy Survey (SINGS; Kennicutt et al. 2003). The 7 mm contours of our low-resolution D-array map are shown overlaid on the IRAC $8 \mu\text{m}$ map in Figure 9. The 7 mm and $8 \mu\text{m}$ emissions have very similar morphologies.

We have compared the corrected flux density in IRAC $8 \mu\text{m}$ and at VLA D-array 7 mm beam by beam. The IRAC $8 \mu\text{m}$ flux density is corrected to remove the stellar emission in the IRAC $8 \mu\text{m}$ band, following Helou et al. (2004). The 7 mm map is convolved to $2''.2 \times 2''.2$ to match the point-spread function (PSF) of IRAC channel 4 ($8 \mu\text{m}$). The $I_{8\mu\text{m}}$ versus $I_{7\text{mm}}$ plot is shown in Figure 10. We limit the data points shown to those with 3σ detection at 7 mm. This process reduces the contribution of nonthermal radio emission which is fainter at high frequency and more extended. The ratio is linear, with $I_{8\mu\text{m}}/I_{7\text{mm}} \approx 45$ and a $I_{8\mu\text{m}}$ zero intercept $\sim 90 \pm 10 \text{ mJy beam}^{-1}$ in $2''.2$ beam. The high correlation of $8 \mu\text{m}$ and 7 mm emission may mean that they are excited by the same relatively strong radiation sources on the $\sim 40 \text{ pc}$ length scale. This is also supported by the spatial correlation between PAH and neon ionic lines found by Beirão et al. 2008. The $I_{8\mu\text{m}}$ that appears even at zero $I_{7\text{mm}}$, about 40% of the total, could be excited by the relatively older population of B stars that do not produce strong radio continuum emission.

Integrating the correlated (above the offset level) $8 \mu\text{m}$ flux density gives about 30 Jy. Our beam-to-beam linear correlation between $I_{8\mu\text{m}}$ and $I_{7\text{mm}}$ suggests that the Lyman continuum rate is

$$N_{\text{lyc}} \sim 2.2 \times 10^{51} \text{ s}^{-1} \left(\frac{D}{\text{Mpc}} \right)^2 \left(\frac{S_{8\mu\text{m}}^{\text{correlated}}}{\text{Jy}} \right), \quad (1)$$

for $I_{8\mu\text{m}} > 0.06 \text{ mJy pc}^{-2}$. Other relations between $S_{8\mu\text{m}}$ and N_{lyc} have been found from work at different wavelengths. Deriving a $P\alpha\alpha$ flux from our N_{lyc} (using $N_{\text{lyc}} = 9.8 \times 10^{63} \text{ s}^{-1} \frac{S_{P\alpha\alpha}}{\text{ergs s}^{-1} \text{ cm}^{-2}}$ from Ho et al. 1990 and Storey & Hummer 1995), the flux density expected from our 7 mm derived N_{lyc} using the Calzetti et al. (2007) relation for $S_{8\mu\text{m}}/S_{P\alpha\alpha}$ would give about a factor of 5 more $S_{8\mu\text{m}}$ than observed. This may not be outside the large scatter in the observed relationship, which Calzetti et al. (2007) discuss. Another prediction of the $8\mu\text{m}$ flux density can be made from the empirical relations $N_{\text{lyc}}/L_{6.2\text{PAH}} \sim 10^{46} \text{ s}^{-1}/L_{\odot}$ (Peeters et al. 2004, based on studies on normal galaxies, starburst galaxies, and H II regions in the Local Group) and $L_{6.2\mu\text{m}}/L_{8.6\mu\text{m}} = 1.5$ (Smith et al. 2007). This would give $S_{8\mu\text{m}}$ about a factor of 10 lower than observed. All relations of the PAH luminosity to N_{lyc} are uncertain and have large scatter because the PAH flux will depend on the geometry of the radiation field, the role of dust, the presence of B stars, and possibly other factors not yet considered. The spatial correlation of the PAH feature and the ionization in M82 is clear; the quantitative relation is not yet so.

PAH emission may be associated with a B star population (Peeters et al. 2004) because the strong UV field of O stars could destroy PAHs. If we constrain the ionization sources of the radio continuum emission in H II regions to be B stars, forcing the initial mass function (IMF) to be deficient in O stars,

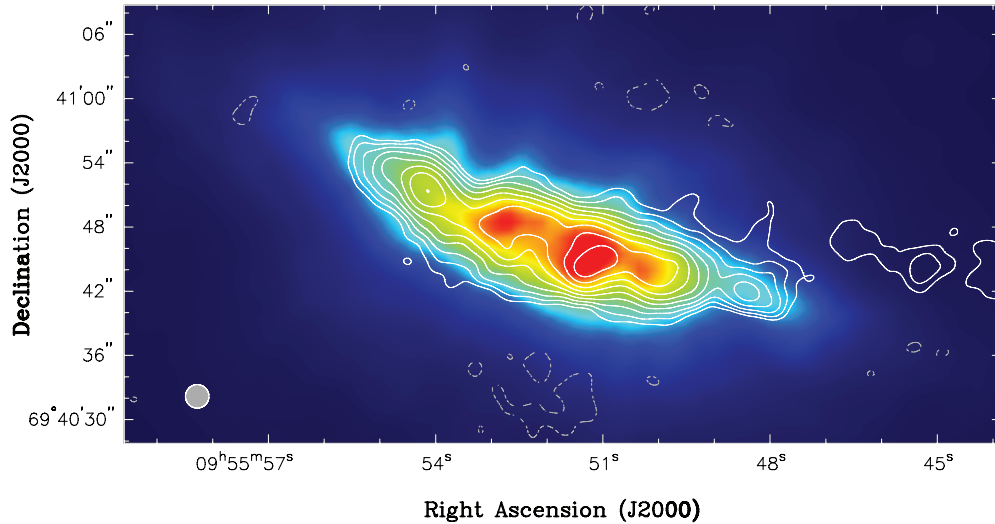


Figure 9. Naturally weighted D-array 7 mm continuum contours overlaid on *Spitzer* IRAC 8 μm map. The contours are $2^{\frac{n}{2}} \times 1.6 \text{ mJy beam}^{-1}$ ($\sim 2\sigma$). The resolutions of both maps are matched to $2''.2$, the size of PSF in IRAC 8 μm .

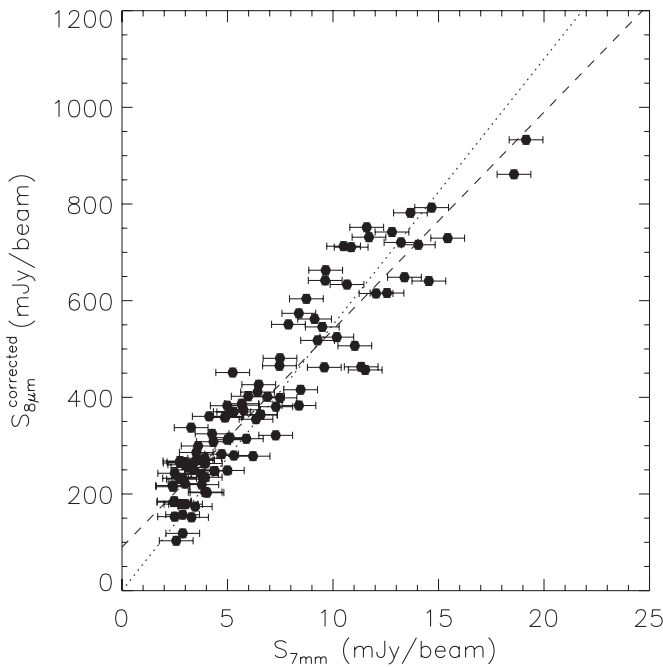


Figure 10. Correlation between flux of PAH feature at 8 μm vs. D-array radio continuum emission at 7 mm. The plot is made with maps of $2''.2$ resolution in $2''.2$ pixels at both wavebands. Each point represents the measurement at an individual pixel. The PAH flux is corrected from IRAC measurements. Data under 3σ are suppressed. The dashed line represent the linear regression result of $S_{8\mu\text{m},\text{corrected}}^{\text{IRAC}} \simeq 45 \times S_{7\text{mm}}^{\text{D-array}} + 90$ in mJy beam^{-1} . The dotted line shows the regression of $S_{8\mu\text{m},\text{corrected}}^{\text{IRAC}} \simeq 55 \times S_{7\text{mm}}^{\text{D-array}}$ in mJy beam^{-1} with a forced zero intercept.

then to produce the observed N_{lyc} would require the total mass of young stars to increase by 2 orders of magnitude relative to a normal IMF. This leads to a star formation rate (SFR) of few hundred solar mass per year for the past 100 Myr, which is highly unlikely.

Why do the radio continuum emission peaks correlate with 8 μm peaks, where the PAH carriers should be destroyed by the UV? It is possible that dust within the H II regions around the massive stars absorbs a significant fraction of the UV flux (Förster Schreiber et al. 2001). Or the production rate of

PAHs may be higher than the destruction. To examine the later scenario, we estimate the lower limit to the number density of hydrogen atoms, n_H , for PAH survival in the UV photon fields observed:

$$n_H > F_{\text{FUV},5.0-13.6\text{eV}} / (H \times c) \quad (2)$$

where c is the speed of light, F_{FUV} is the photon flux rate [photon $\text{cm}^{-2} \text{s}^{-1}$] for photons with energy between 5–13.6 eV, and the dimensionless H is defined as the Habing photodissociation parameter,⁸ following Section 12.7 of Dopita & Sutherland (2003). Dopita & Sutherland (2003) suggest $H \sim 0.05$, an upper limit from line-of-sight average from observation (Allain et al. 1996), for PAH molecule destruction. The Starburst99 code (with Salpeter IMF) gives a ratio of the far UV ionizing flux, N_{FUV} , to N_{lyc} of $N_{\text{FUV}}/N_{\text{lyc}} \sim 3$ for O-type dominated stellar population, thus we find

$$F_{\text{FUV}}[\text{cm}^{-2} \text{s}^{-1}] \sim 1.3 \times 10^{12} \frac{I_{7\text{mm}}}{\text{mJy beam}^{-1}}. \quad (3)$$

So the lower limit of hydrogen atom number density, $n_H = 900 \times (\frac{I_{7\text{mm}}}{\text{mJy beam}^{-1}}) \text{ cm}^{-3}$ for PAH survival in the localized region where $I_{7\text{mm}}$ is observed. In M82, the peak 7 mm VLA flux density in a $\sim 2''$ beam ~ 5 –20 mJy, requiring $n_H > 5 \times 10^3 \text{ cm}^{-3}$. If $H \sim 0.005$ which ensures the PAH survival in the PDRs but not inside the ionized media (Dopita et al. 2005), $n_H > 5 \times 10^4 \text{ cm}^{-3}$ is required to supply the observed PAH, close to the critical density for HCN excitation. This agrees with the good correlation between intensities of PAH with HCN emission in M82 found in $2.4''$ beam (not shown in this paper).

5. STAR FORMATION HISTORY AND EFFICIENCY

5.1. Star Formation and its Recent History in M82

Förster Schreiber et al. (2003) proposed the star formation history of selected starburst regions in M82 based on ISO MIR imaging and spectroscopy for $\lambda = 1$ –45 μm . For the central $16'' \times 10''$ region, they found star formation had peaked near 5 and 9 Myr ago with amplitudes of 6.3 and 18.5 $M_{\odot} \text{ yr}^{-1}$,

⁸ “ H ” represents the ratio of local F_{FUV} photo density and the density of atomic hydrogen.

respectively, and had dipped to less than $0.1 M_{\odot} \text{ yr}^{-1}$ at 6 Myr or so. Previously Förster Schreiber et al. (2001) had commented on the lack of the Wolf–Rayet (W–R) spectral signatures in M82, which may be due to high extinction toward the “young” star-forming regions (3–6 Myr) where the W–R stars live, but could also reflect the SFR dip near 3+ Myr ago. Our observations suggest that high extinction is the reason for the absence of WR features, since all of the young radio free–free sources are found in heavily visually obscured regions.

The integrated flux density at 7 mm of the full region Förster Schreiber et al. (2001, 2003) mapped is about 340 mJy in the low-resolution 7 mm map. This equates to a total mass in young stars of $1.3 \times 10^7 M_{\odot}$ formed within the average lifetime of O stars of 1–3 Myr, for a Salpeter IMF of 1–100 M_{\odot} . The contribution of the previous two starburst events at 5 Myr and 9 Myr to 7 mm flux density would be negligible. The average SFR over this region in about the past 3 Myr (before O stars enter the W–R phase), based on inferred total mass of young star population from 7 mm flux density, is thus estimated as $4 M_{\odot} \text{ yr}^{-1}$ (Salpeter IMF of 1–100 M_{\odot}), in agreement with the radio recombination line study by Rodriguez-Rico et al. (2004), and with the rate estimated based on numbers of radio SNRs (Huang et al. 1994; Muxlow et al. 1994; Kronberg et al. 2000; Fenech et al. 2008).

5.2. Molecular Gas and Star Formation Efficiency

Our 7 mm continuum images give a picture of where the young star-forming regions are in M82, particularly the compact 7 mm sources that are likely very young embedded clusters. What is the spatial relation of these sources to the molecular gas? Is there evidence in the spatial distribution for how the star formation was triggered?

We can estimate M_{star} , the mass of new stars formed, from L_{IR} , M_{gas} , the total mass of gas, from L_{CO} , and the mass of dense (M_{dense} ; $n_{\text{H}_2} > 10^4 \text{ cm}^{-3}$) gas from L_{HCN} . The dense gas fraction is therefore $M_{\text{dense gas}}/M_{\text{gas}}$ and the SFE, the fraction of total gas converted to newly formed stars, is $M_{\text{star}}/(M_{\text{star}} + M_{\text{gas}})$. This is the SFE for the current generation of stars (i.e., on timescales of a few Myr). We convert our observed $S_{7\text{mm}}$ in lower-resolution map to L_{OB} in the $2''.7$ beam, take that L_{OB} to be L_{IR} , and find M_{star} from $M_{\text{star}} = 1.5 \times 10^{-3} L_{\text{IR}} M_{\odot} L_{\odot}^{-1}$, which assumes an O star-dominated population with Salpeter IMF between 1 M_{\odot} and 100 M_{\odot} . Since we are using the total 7 mm flux density for this computation rather than the thermal 7 mm flux density, the L_{OB} and L_{IR} values could be overestimated by 30% due to the nonthermal contribution. The full translation is uncertain by a factor of 3, mainly corresponding to the difference in lower mass cutoff in IMF. We find the dense gas mass fraction from $I_{\text{HCN}}/I_{\text{CO}}$. For the molecular gas mass, we adopt the conversion of $M_{\text{dense gas}}(\text{H}_2) = 10 L_{\text{HCN}} M_{\odot} (\text{K km s}^{-1} \text{ pc}^2)^{-1}$, and $M_{\text{gas}}(\text{H}_2) = 4.8 L_{\text{CO}} M_{\odot} (\text{K km s}^{-1} \text{ pc}^2)^{-1}$ from Gao & Solomon (2004b). These conversions for molecular gas are uncertain by a factor of 2–3, discussed in Gao & Solomon (2004b).

In Figure 8, we plot the observables $L_{\text{IR}}/L_{\text{CO}}$ versus $L_{\text{HCN}}/L_{\text{CO}}$. The corresponding SFEs against the dense gas fraction (DGF) are shown on the top and right. The data points of M82 represent the results on a $2.7''$ scale (or ~ 46 pc). We show local normal spirals, luminous infrared galaxies (LIRGs), ultraluminous infrared galaxies (ULIRGs), and high- z starburst galaxies from Gao et al. (2007) spirals, on the same plot. The SFE and DGF track in M82 roughly as they do in all sources, although the size scales of the observations can be very different. All M82 data area lie under the SFE:DGF = 1:1 line, which

suggests that less than 50% of the molecular gas has been turned into stars. Most of the data points lie above the SFE:DGF = 1:10 line, implying a limit of $\sim 10\%$ SFE for dense molecular gas.

6. REMARKS ON COMPACT NON-THERMAL SOURCES

We have detected five nonthermal sources with flux densities higher than 5σ . Their flux densities at wavelengths between 7 mm and 18 cm in $0''.2 \times 0''.2$ beams are listed in Table 2 and plotted in Figure 3. We overlay on the measured SED the best fit to a model of a single power law with free–free absorption.

The model results are shown in Table 3. About one-third of the compact 7 mm sources we detected (Table 1) are nonthermal. These sources have been known for some time and are believed to be SNRs (Kronberg & Sramek 1985). However, they do not decline with time as expected, so it has been suggested that they may be wind-driven bubbles instead (Seaquist & Stanković 2007).

6.1. 43.992+59.70: Potential AGN in M82?

The brightest 7 mm continuum compact source is 43.992+59.70, which has been suggested to be the nucleus of M82 (Kronberg & Wilkinson 1975). On the basis of European VLBI Network and VLA images, Wills et al. (1999a) suggest this source could be a candidate for the AGN in M82 based on the jet-like feature, although they detected only the northern part. The study of two radio OH satellite lines also suggests the OH features of this source could be associated with a circumnuclear disk or torus (Seaquist et al. 1997). 43.992+59.70 is also within $3''$ of the $2 \mu\text{m}$ peak of M82 (Lester et al. 1990) that is presumably in the center of the mass distribution. In addition, [Ne II] line (Achtermann & Lacy 1995), and OH maser kinematics (Seaquist et al. 1997), molecular gas investigation (Seaquist et al. 1997), and radio recombination line results (Rodriguez-Rico et al. 2004) also suggest that this source is close to the dynamical center of M82, which supports the AGN scenario.

The suggestion that 43.992+59.70 is an AGN also can be tested by looking for variability. Long-term radio flux monitoring by Kronberg et al. (2000) suggests that the source has a stable flux density, with variability $\leq 5\%$, which is the uncertainty in the absolute flux scale calibration. Our 7 mm flux density is about 63% of the archival centimeter-wave SED model’s prediction. It is possible that 43.992+59.70 is variable at the current epoch, or that the spectrum is not a power law to 7 mm.

A discrepancy from the AGN picture is that *Chandra* high-resolution X-ray images do not show 43.992+59.70 as a strong source. Also, another argument against the AGN nature of 43.992+59.70 can be based on the recent high-resolution VLBI and MERLIN images of this source (McDonald et al. 2001; Fenech et al. 2008), where it has a resolved round structure, consistent with an SNR as suggested by its spectral index ($\alpha \sim -0.5$) (Huang et al. 1994). However, the measured 7 mm flux density appears to miss a significant amount of flux density from the SED model of SNR, and it is hard to match the 7 mm flux density into the SNR picture.

This bright nonthermal source also coincides with a compact $Pa\alpha$ and $1.644 \mu\text{m}$ [Fe II] emitter. Seaquist & Stanković (2007) modeled the radio emission of nonthermal sources in M 82, including this one, as wind-driven bubbles. This scenario hypothesizes that nonthermal synchrotron emitting particles are produced at the shock between the wind of young star clusters and hot bubble gas. However, Fenech et al. (2008) measure the expansion velocity of this source to be at 2700 km s^{-1} ,

which is about 50 times higher than the expect wind-driven shell (Seaquist & Stanković 2007), and it is more closer to the free-expanding SNR.

In summary, these three models involving AGN, SNR, and nonthermal bubble of a young cluster could all explain the strong 7 mm emission of 43.992+59.70. Despite some suggestive dynamical evidences, the morphology and expansion revealed by the VLBI and MERLIN work strongly indicate that the source is an SNR. However, the SNR scenario could not explain the decline of flux density at 7 mm from the expectation value of SED modeling. The nature of this source might be still open to debate.

6.2. Intermediate Black Hole Candidate M82 X-1 (CXO M82 J095550.2+694047)

Matsumoto et al. (2001) reported 9 X-ray sources in M82. The source CXO M82 J095550.2+694047, or M82 X-1 ($09^{\text{h}}55^{\text{m}}50^{\text{s}}.2$, $+69^{\circ}40'47''$; Matsumoto et al. 2001), has been categorized as an ultraluminous X-ray source (ULX) and a 54 mHz quasiperiodic oscillation has been found in X-ray by Strohmayer & Mushotzky (2003) and a possible 62 day X-ray luminosity variation by Kaaret et al. (2006). It is suggested to host an intermediate mass black hole (Ebisuzaki et al. 2001; Portegies Zwart et al. 2004). Many attempts have been made to find a radio counterpart of M82 X-1 (Matsumoto et al. 2001; Körding et al. 2005; Kaaret et al. 2006). The source 41.30+59.6 or 41.5+59.7 has been suggested to be a possible counterpart. We did not detect a significant radio counterpart of M82 X-1 at 7 mm to a limit of $0.7 \text{ mJy } \text{bm}^{-1}$. The SEDs of the nearby 7 mm sources 40.933+58.98 and 41.628+58.01 are clearly thermal and are also not candidates for the radio counterpart of M82 X-1.

6.3. Variable Compact Sources

The flux density of nonthermal source 41.942+57.62 (41.9+58 in Kronberg et al. 1985 and Kronberg et al. 2000) at 7 mm is significantly below the power-law model (Figure 3). This source is known to vary (Kronberg & Sramek 1985); its flux density declines at $\sim 8.4\%$ – 8.8% per year at ~ 5 GHz, as has been shown and discussed by several authors (Kronberg & Sramek 1992; Allen 1999; Kronberg et al. 2000; Muxlow et al. 2005; Fenech et al. 2008). The cm data listed in Table 2 and plotted in Figure 3 were obtained before 1996 (Allen 1999). Based on the epoch-corrected 1993 values of Allen & Kronberg (1998) for the flux density of 41.942+57.62, and for a spectral index of -0.72 (from best-fit result without 7 mm data point), we estimate that the flux density of 41.942+57.62 would have been 8 mJy at 7 mm in 1993, three times higher than the observed value. This is consistent with a decline of 8.4% /year found at 5 GHz.

Singer et al. (2004) first reported the supernova SN2004am ($9:55:46.61$; $+69:40:48.1$), which was classified spectroscopically as Type II (Mattila et al. 2004). Beswick et al. (2004) report 3σ upper limits for this source of $0.34 \text{ mJy } \text{bm}^{-1}$ (8.4 GHz) and $1 \text{ mJy } \text{bm}^{-1}$ (15 GHz) on 2003 November 14. The null detection in their MERLIN observations at 5 GHz on 2004 March 9 gave an upper limit of $0.18 \text{ mJy } \text{bm}^{-1}$ (3σ), and suggested that the SN2004am should reach the radio emission peak with a significant delay (up to about one year). We can place a 3σ upper limit of $S_{7\text{mm}} = 0.6 \text{ mJy } \text{bm}^{-1}$ to the 7 mm flux density of SN2004am in our observation of 2005 April 3.

There are at least seven known sources for which the 7 mm flux density predicted from their centimeter-wave flux densities

should be larger than 1 mJy (5σ – 7σ). They are 40.68+551, 43.82+628, 45.41+637, 45.48+647, 46.18+677, 46.52+639, and 47.37+680. The last four of these are at greater than $20''$ from the phase center where the noise level is a factor of 2 higher than elsewhere and these may be down in the noise. Sources 40.68+551 and 43.82+628 are, however, within the central primary beam in a low-noise region. Both 40.68+551 and 43.82+628 are SNRs. Source 40.68+551 has minor variability in the long-term radio continuum flux experiment of Kronberg et al. (2000), but no variability of 43.82+628 has been reported, and this may be the first indication.

For three of the 7 mm sources (39.659+55.73, 43.992+59.70, and 45.153+61.34) the 7 mm flux densities are stronger at the epoch of our observation (2005) with $\lesssim 0''.2$ beam than at year 2000–2001 in the observation of Rodriguez-Rico et al. (2004) with a $0''.6$ beam. The flux density differences are not conclusive ($\sim 2\sigma$ of the C-array), but suggest that these sources may be varying. The latter two sources are believed to be SNRs, based on their radio SEDs. Neither of them vary strongly at 6 cm in the 12 year monitoring program of Kronberg et al. (2000) between 1981 and 1992. Source 39.659+55.73 is known to vary at 6 cm, fluctuating 20% continuously during this time period. But we have characterized this source as an H II region based on its rising spectrum, and it therefore should not vary. This source might be associated with a wind-driven bubble, as suggested for the nonthermal sources by Seaquist & Stanković (2007).

7. CONCLUSIONS

We present 7 mm VLA continuum maps of the starburst in M82 at two resolutions, $0''.2$ (B-configuration) and $2''$ (D-configuration). We recover essentially all of the 7 mm flux density of M82 in the lower-resolution D-array map. An estimated 2/3 of this flux density is thermal free–free emission from the starburst. We detect less than 10% of the total 7 mm flux density in the high-resolution B-array map, which is sensitive to only bright, compact emission sources.

We identify 14 compact sources greater than $0.5 \text{ mJy } \text{bm}^{-1}$ (5σ) in the high-resolution image, and have constructed SEDs using archival VLA data. Nine of the compact sources are compact H II regions, with emission measures $EM > 10^8 \text{ cm}^{-6}$ pc, sizes of $\lesssim 3$ pc, and rms densities $(n_e^2)^{1/2} \gtrsim 3000$. These compact sources are located in regions of heavy visual obscuration, with no associated NIR continuum counterparts. This could explain the lack of W–R features in M82. Our detection limit is $N_{\text{Iyc}} \sim 0.6 \times 10^{51} \text{ s}^{-1}$, so the smallest of these clusters has ~ 100 O stars, and the largest, ~ 1200 O stars ($N_{\text{Iyc}} \sim 10^{53} \text{ s}^{-1}$). The detected compact thermal sources account for $\sim 6\%$ of the total 7 mm free–free flux density. Since the maps detect only the most luminous compact H II regions, this ratio should be higher if fainter ones are taken into account. We therefore infer that the compact H II region phase in M82 must last at least 6% of the H II region lifetime, ~ 1 Myr or longer.

In addition to the compact H II regions, the high-resolution map reveals extended ($2''$, or 30 pc) regions of free–free emission with $EM > 10^7 \text{ cm}^{-6}$ pc. The comparison of intensity (EM) and flux (N_{Iyc}) suggests that these regions are likely to be nonspherical in geometry. We suggest two possibilities, either these regions indicate regions of distributed star formation, with many small H II regions possibly reflecting enhanced star formation at the ends of the bar in M82, or these regions are sheet-like structures, possibly caused by winds or supernovae.

We have compared lower-resolution 7 mm VLA maps to maps of molecular gas tracers and dust. The good correlation between the 7 mm emission and *Spitzer* IRAC Channel 4 map (dominated by 8 μm PAH features) suggests a relation $N_{\text{lyc}} \sim 2.2 \times 10^{51} \text{ s}^{-1} \left(\frac{D}{\text{Mpc}}\right)^2 \left(\frac{S_{8\mu\text{m}}}{\text{Jy}}\right)$, for intensities $I_{8\mu\text{m}} > 0.06 \text{ mJy pc}^{-2}$. This indicates that the PAH feature is a good tracer of star formation in M82, although we obtain a different relation between N_{lyc} and the 8 μm emission than previous work.

The correlation of 7 mm emission and molecular gas tracers (CO and HCN) at 2'' scales is excellent, indicating that the relation of star formation and HCN emission found on global scales by (Gao & Solomon 2004a) holds down to GMC scales. We estimate that the SFE in M82 on GMC scales is $\sim 1\% - 10\%$, similar to Galactic values, and that the regions of highest SFE also have the highest fraction of dense ($n_{\text{H}_2} \gtrsim 10^4 \text{ cm}^{-3}$) gas.

The authors gratefully acknowledge the anonymous referee for the valuable comments. We also thank Almudena Alonso-Herrero, Sarah Lipsy, and Peter Schilke for their generosity in providing their data. C.W.T. appreciates helpful discussions with Yu Gao. Some of the data used in this paper were obtained from the Multimission Archive at the Space Telescope Science Institute (MAST). STScI is operated by the Association of Universities for Research in Astronomy, Inc., under NASA contract NAS5-26555. This research has also made use of the NASA/IPAC Extragalactic Database (NED) and the NASA/IPAC Infrared Science Archive (IRSA) which are operated by the Jet Propulsion Laboratory, California Institute of Technology, under contract with the National Aeronautics and Space Administration.

REFERENCES

- Achtermann, J. M., & Lacy, J. H. 1995, *ApJ*, **439**, 163
 Allain, T., Leach, S., & Sedlmayr, E. 1996, *A&A*, **305**, 602
 Allen, M. L. 1999, Ph.D. thesis, Univ. Toronto
 Allen, M. L., & Kronberg, P. P. 1998, *ApJ*, **502**, 218
 Alonso-Herrero, A., Rieke, G. H., Rieke, M. J., & Kelly, D. M. 2003, *AJ*, **125**, 1210
 Beck, S. C., Turner, J. L., Langland-Shula, L. E., Meier, D. S., Crosthwaite, L. P., & Gorjian, V. 2002, *AJ*, **124**, 2516
 Bennett, C. L., et al. 2003, *ApJS*, **148**, 97
 Beswick, R. J., Muxlow, T. W. B., Argo, M. K., & Pedlar, A. 2004, *IAU Circ.*, **8332**, 2
 Beswick, R. J., et al. 2006, *MNRAS*, **369**, 1221
 Beirão, P., et al. 2008, *ApJ*, **676**, 304
 Calzetti, D., et al. 2007, *ApJ*, **666**, 870
 Carlstrom, J. E., & Kronberg, P. P. 1991, *ApJ*, **366**, 422
 Condon, J. J. 1992, *ARA&A*, **30**, 575
 de Grijs, R. 2001, *Astron. Geophys.*, **42**, 12
 de Pree, C. G., Rodriguez, L. F., & Goss, W. M. 1995, *RevMexAA*, **31**, 39
 Dopita, M. A., & Sutherland, R. S. 2003, *Astrophysics of the Diffuse Universe*, *Astronomy and Astrophysics Library* (Berlin: Springer)
 Dopita, M. A., et al. 2005, *ApJ*, **619**, 755
 Ebisuzaki, T., et al. 2001, *ApJ*, **562**, L19
 Engelbracht, C. W., et al. 2006, *ApJ*, **642**, L127
 Fenech, D. M., Muxlow, T. W. B., Beswick, R. J., Pedlar, A., & Argo, M. K. 2008, *MNRAS*, **391**, 1384
 Förster Schreiber, N. M., Genzel, R., Lutz, D., Kunze, D., & Sternberg, A. 2001, *ApJ*, **552**, 544
 Förster Schreiber, N. M., Genzel, R., Lutz, D., & Sternberg, A. 2003, *ApJ*, **599**, 193
 Freedman, W. L., et al. 1994, *ApJ*, **427**, 628
 Gao, Y., Carilli, C. L., Solomon, P. M., & Vanden Bout, P. A. 2007, *ApJ*, **660**, L93
 Gao, Y., & Solomon, P. M. 2004a, *ApJ*, **606**, 271
 Gao, Y., & Solomon, P. M. 2004b, *ApJS*, **152**, 63
 Greve, A., Wills, K. A., Neininger, N., & Pedlar, A. 2002, *A&A*, **383**, 56
 Helou, G., et al. 2004, *ApJS*, **154**, 253
 Ho, P. T. P., Beck, S. C., & Turner, J. L. 1990, *ApJ*, **349**, 57
 Hollenbach, D. J., & Tielens, A. G. G. M. 1997, *ARA&A*, **35**, 179
 Huang, Z. P., Thuan, T. X., Chevalier, R. A., Condon, J. J., & Yin, Q. F. 1994, *ApJ*, **424**, 114
 Kaaret, P., Simet, M. G., & Lang, C. C. 2006, *ApJ*, **646**, 174
 Kennicutt, R. C. Jr., et al. 2003, *PASP*, **115**, 928
 Keto, E., Ho, L. C., & Lo, K.-Y. 2005, *ApJ*, **635**, 1062
 Körding, E., Colbert, E., & Falcke, H. 2005, *A&A*, **436**, 427
 Kronberg, P. P., Biermann, P., & Schwab, F. R. 1985, *ApJ*, **291**, 693
 Kronberg, P. P., Pritchett, C. J., & van den Bergh, S. 1972, *ApJ*, **173**, L47
 Kronberg, P. P., & Sramek, R. A. 1985, *Science*, **227**, 28
 Kronberg, P. P., & Sramek, R. A. 1992, X-ray Emission from Active Galactic Nuclei and the Cosmic X-ray Background (Tucson, AZ: NRAO)
 Kronberg, P. P., Sramek, R. A., Birk, G. T., Dufton, Q. W., Clarke, T. E., & Allen, M. L. 2000, *ApJ*, **535**, 706
 Kronberg, P. P., & Wilkinson, P. N. 1975, *ApJ*, **200**, 430
 Larkin, J. E., Graham, J. R., Matthews, K., Soifer, B. T., Beckwith, S., Herbst, T. M., & Quillen, A. C. 1994, *ApJ*, **420**, 159
 Lester, D. F., Gaffney, N., Carr, J. S., & Joy, M. 1990, *ApJ*, **352**, 544
 Lipsy, S. J., & Plavchan, P. 2004, *ApJ*, **603**, 82
 Loiseau, N., Nakai, N., Sofue, Y., Wielebinski, R., Reuter, H.-P., & Klein, U. 1990, *A&A*, **228**, 331
 Matsumoto, H., Tsuru, T. G., Koyama, K., Awaki, H., Canizares, C. R., Kawai, N., Matsushita, S., & Kawabe, R. 2001, *ApJ*, **547**, L25
 Matsumoto, H., Tsuru, T. G., Matsushita, S., Kawabe, R., & Prestwich, A. 2000, *BAAS*, **32**, 751
 Matsushita, S., Kawabe, R., Kohno, K., Matsumoto, H., Tsuru, T. G., & Vila-Vilaró, B. 2005, *ApJ*, **618**, 712
 Matsushita, S., Kawabe, R., Matsumoto, H., Tsuru, T. G., Kohno, K., Morita, K. I., Okumura, S. K., & Vila-Vilaró, B. 2000, *ApJ*, **545**, L107
 Mattila, S., Meikle, W. P. S., Groeningson, P., Greimel, R., Schirmer, M., Acosta-Pulido, J. A., & Li, W. 2004, *IAU Circ.*, **8299**, 2
 Mayya, Y. D., Carrasco, L., & Luna, A. 2005, *ApJ*, **628**, L33
 McCrady, N., Gilbert, A. M., & Graham, J. R. 2003, *ApJ*, **596**, 240
 McDonald, A. R., Muxlow, T. W. B., Pedlar, A., Garrett, M. A., Wills, K. A., Garrington, S. T., Diamond, P. J., & Wilkinson, P. N. 2001, *MNRAS*, **322**, 100
 McDonald, A. R., Muxlow, T. W. B., Wills, K. A., Pedlar, A., & Beswick, R. J. 2002, *MNRAS*, **334**, 912
 McLeod, K. K., Rieke, G. H., Rieke, M. J., & Kelly, D. M. 1993, *ApJ*, **412**, 111
 Melo, V. P., Muñoz-Tuñón, C., Maíz-Apellániz, J., & Tenorio-Tagle, G. 2005, *ApJ*, **619**, 270
 Muxlow, T. W. B., Pedlar, A., Beswick, R. J., Argo, M. K., O'Brien, T. J., Fenech, D., & Trotman, W. 2005, *Mem. Soc. Astron. Ital.*, **76**, 586
 Muxlow, T. W. B., Pedlar, A., Wilkinson, P. N., Axon, D. J., Sanders, E. M., & de Bruyn, A. G. 1994, *MNRAS*, **266**, 455
 Nakai, N., Hayashi, M., Handa, T., Sofue, Y., Hasegawa, T., & Sasaki, M. 1987, *PASJ*, **39**, 685
 Neininger, N., Guélin, M., Klein, U., Garcia-Burillo, S., & Wielebinski, R. 1998, *A&A*, **339**, 737
 O'Connell, R. W., & Mangano, J. J. 1978, *ApJ*, **221**, 62
 Pedlar, A., Muxlow, T. W. B., Garrett, M. A., Diamond, P., Wills, K. A., Wilkinson, P. N., & Alef, W. 1999, *MNRAS*, **307**, 761
 Peeters, E., Spoon, H. W. W., & Tielens, A. G. G. M. 2004, *ApJ*, **613**, 986
 Portegies Zwart, S. F., Baumgardt, H., Hut, P., Makino, J., & McMillan, S. L. W. 2004, *Nature*, **428**, 724
 Rieke, G. H., Lebofsky, M. J., Thompson, R. I., Low, F. J., & Tokunaga, A. T. 1980, *ApJ*, **238**, 24
 Rodriguez-Rico, C. A., Viallefond, F., Zhao, J.-H., Goss, W. M., & Anantharamaiah, K. R. 2004, *ApJ*, **616**, 783
 Sakai, S., & Madore, B. F. 1999, *ApJ*, **526**, 599
 Seaquist, E. R., Bell, M. B., & Bignell, R. C. 1985, *ApJ*, **294**, 546
 Seaquist, E. R., Frayer, D. T., & Frail, D. A. 1997, *ApJ*, **487**, L131
 Seaquist, E. R., & Stanković, M. 2007, *ApJ*, **659**, 347
 Shen, J., & Lo, K. Y. 1995, *ApJ*, **445**, L99
 Simon, M., Simon, T., & Joyce, R. R. 1979, *ApJ*, **227**, 64
 Singer, D., Pugh, H., & Li, W. 2004, *IAU Circ.*, **8297**, 2
 Smith, L. J., & Gallagher, J. S. 2001, *MNRAS*, **326**, 1027
 Smith, L. J., Westmoquette, M. S., Gallagher, J. S., O'Connell, R. W., Rosario, D. J., & de Grijs, R. 2006, *MNRAS*, **370**, 513
 Smith, J. D. T., et al. 2007, *ApJ*, **656**, 770
 Stevens, I. R., Read, A. M., & Bravo-Guerrero, J. 2003, *MNRAS*, **343**, L47
 Storey, P. J., & Hummer, D. G. 1995, *MNRAS*, **272**, 41
 Strohmayer, T. E., & Mushotzky, R. F. 2003, *ApJ*, **586**, L61
 Telesco, C. M. 1988, *ARA&A*, **26**, 343

- Telesco, C. M., Joy, M., Dietz, K., Decher, R., & Campins, H. 1991, [ApJ](#), **369**, [135](#)
- Turner, J. L., Beck, S. C., Crosthwaite, L. P., Larkin, J. E., McLean, I. S., & Meier, D. S. 2003, [Nature](#), **423**, [621](#)
- Turner, J. L., Beck, S. C., & Ho, P. T. P. 2000, [ApJ](#), **532**, [L109](#)
- Turner, J. L., & Ho, P. T. P. 1983, [ApJ](#), **268**, [L79](#)
- Turner, J. L., & Ho, P. T. P. 1994, [ApJ](#), **421**, [122](#)
- Turner, J. L., Ho, P. T. P., & Beck, S. C. 1998, [AJ](#), **116**, [1212](#)
- Unger, S. W., Pedlar, A., Axon, D. J., Wilkinson, P. N., & Appleton, P. N. 1984, [MNRAS](#), **211**, [783](#)
- Weiß, A., Walter, F., Neininger, N., & Klein, U. 1999, [A&A](#), **345**, [L23](#)
- Willner, S. P., Soifer, B. T., Russell, R. W., Joyce, R. R., & Gillett, F. C. 1977, [ApJ](#), **217**, [L121](#)
- Wills, K. A., Pedlar, A., Muxlow, T. W. B., & Stevens, I. R. 1999, [MNRAS](#), **305**, [680](#)
- Wills, K. A., Pedlar, A., Muxlow, T. W. B., & Wilkinson, P. N. 1997, [MNRAS](#), **291**, [517](#)
- Wills, K. A., Redman, M. P., Muxlow, T. W. B., & Pedlar, A. 1999, [MNRAS](#), **309**, [395](#)
- Wu, J., Evans, N. J., II, Gao, Y., Solomon, P. M., Shirley, Y. L., & Vanden Bout, P. A. 2005, [ApJ](#), **635**, [L173](#)
- Yun, M. S., Ho, P. T. P., & Lo, K. Y. 1993, [ApJ](#), **411**, [L17](#)